

Beating Down Cosmic Redshift Drift

Alex G. Kim, Eric V. Linder, ...

February 7, 2014

ABSTRACT

Redshift drift provides a direct kinematic measurement of cosmic acceleration but it occurs with a characteristic time scale of a Hubble time. Thus redshift observations with a challenging precision of 10^{-9} require a 10 year time span to obtain a signal-to-noise of 1. We discuss theoretical and experimental approaches to address this challenge, potentially requiring less observer time and having greater immunity to common systematics. On the theoretical side we explore allowing the universe, rather than the observer, to provide long time spans; speculative methods include radial baryon acoustic oscillations, cosmic pulsars, and strongly lensed quasars. On the experimental side, we explore beating down the redshift precision using differential interferometric techniques, including externally dispersed interferometers and spatial heterodyne spectroscopy. Low redshift emission line galaxies are identified as having high cosmology leverage and systematics control, with an 8 hour exposure on a 10-meter telescope (1000 hours of exposure on a 40-meter telescope) potentially capable of measuring redshifts to a precision of 2×10^{-9} ($\sim 5 \times 10^{-11}$).

1. Introduction

Our universe is dynamical, i.e. the metric evolves or more simply the scale factor of the universe changes with time, hence $a(t)$. This kinematic effect gives rise to the cosmic redshift of light from distant sources. Moreover, since the expansion rate itself evolves, in all but a coasting, Milne universe, the redshift itself will shift. This redshift drift was introduced by Sandage ? and McVittie ? in the early 1960s and revisited in the 1980s and 1990s; see the textbook summary in ?.

Just as redshift is direct, kinematical evidence for cosmic expansion, redshift drift is likewise for cosmic acceleration. This directness is an attractive feature, so even if such a cosmic probe cannot reach the accuracy on cosmological parameter estimation of, say, distance or growth of structure probes, it is worthwhile to explore possibilities to carry it out.

Conventionally, this is thought of in a brute force approach: stare at an object for a long time and wait to measure the change in its redshift. Since the time scale for an order unity variation is the characteristic time scale of the expansion, the Hubble time of $\sim 10^{10}$ y, this requires fantasti-

cally precise measurements of redshift stable over the observing period. Moreover, any other time variation in the metric that is not linear gives a competing effect. From the Principle of Equivalence, any acceleration of the source or change in gravity along the line of sight acts as a systematic contribution.

Here we explore two parallel tracks to make this cosmological probe more viable. One is exploring theoretical ideas for letting the universe do the difficult work for us, by taking advantage of source redshifts delivered to us at effectively different epochs and of differential rather than absolute measurements. The second involves experimental approaches to improve the brute force precision, while again using differential measurements to ameliorate instrumental systematics. As with any probe, systematics are a key concern so any method that may enable better control of them is important to consider.

In Sec. 2 we review the basic redshift drift and the plethora of systematics that confront it, as well as the potential cosmological leverage. Section 3 outlines three theoretical alternatives to the brute force approach, each with their own advantages and speculative aspects. We turn to some inno-

vative experimental approaches in Sec. 4, which may offer improvements in precision and systematics, and conclude in Sec. 7.

2. Redshift Drift and Systematics

In back to back articles published in 1962, McVittie ? and Sandage ? laid out the basics of redshift drift. Since the cosmic redshift $z = a^{-1} - 1$, then the dependence $a(t)$ of the source with respect to the observer necessarily implies that z changes with time as well. Following the approach in ?, we have

$$\begin{aligned} \frac{dz}{dt_0} &= \frac{d}{dt_0} \left[\frac{a(t_0)}{a(t_e)} - 1 \right] = \frac{\dot{a}(t_0) - \dot{a}(t_e)}{a(t_e)} \quad (1) \\ &= (1+z)H_0 - H(z), \quad (2) \end{aligned}$$

where t_0 is the observing time, t_e the signal emission time, and $H = \dot{a}/a$ the Hubble expansion rate.

The form involving a difference between \dot{a} 's makes clear that this arises from acceleration (positive or negative). Only a universe where $\dot{a} = \text{constant}$, i.e. $a \propto t$, has no redshift drift. This is a Milne universe, which is conformal to a Minkowski spacetime, and so the Principle of Equivalence assures us that a universe without gravity has no acceleration, and vice versa. We emphasize the kinematic aspect of the redshift drift: its nonzero value directly indicates acceleration, with no need to know the dynamics, i.e. the specific functional dependence $a(t)$. Only when we want to compare to a particular model, e.g. so much matter density and so much dark energy density with some equation of state, do we need to know $a(t)$.

At high redshift we expect the universe to be decelerating, and hence the drift should be negative. When the universe begins to accelerate (speed up) under the influence of dark energy in recent times, however, then the drift will change to positive. Thus the hope is to map out the influence of dark energy, and its equation of state, by accurate measurements of the redshift drift.

One fly in the ointment is that in fact the observed redshift $z \neq a^{-1} - 1$. The full relativistic expression is

$$1+z = \frac{(g_{\mu\nu}k^\mu u^\nu)_e}{(g_{\mu\nu}k^\mu u^\nu)_o}, \quad (3)$$

with the redshift drift obtaining contributions from not only the homogeneous expansion in the metric, but 1) inhomogeneous gravitational potentials, 2) deviations in the photon four-momentum k^μ due to inhomogeneities, and 3) time variation of the source four-velocity u^ν , i.e. peculiar accelerations.

The full expression for the redshift drift including metric and geodesic effects but not peculiar acceleration is

$$\begin{aligned} \frac{dz}{dt_o} &= \frac{\dot{a}_o - \dot{a}_e}{a_e} \quad (4) \\ &+ 2[\dot{\psi}_e - (1+z)\dot{\psi}_o] + \frac{2}{a_e}\partial_1(\psi_e - \psi_o) \\ &- (\dot{\psi}_e - \dot{\phi}_e) + (1+z)(\dot{\psi}_o - \dot{\phi}_o) \\ &- H(z)(\phi_o - \phi_e) + H_0(1+z)[a_o k_o^0]^{(1)}, \end{aligned}$$

where ψ and ϕ are the metric gravitational potentials. These terms are discussed in detail in ?; most are smaller than, though some are comparable to (especially for relativistic systems), peculiar accelerations.

As for peculiar accelerations, using $\vec{\nabla}\psi \sim \dot{u}$, the contribution is

$$\dot{u} \sim \frac{\psi}{L} \sim H \frac{H^{-1}}{L} \psi \sim H \left(\frac{40 \text{ kpc}}{L} \right) \left(\frac{\psi}{10^{-5}} \right), \quad (5)$$

where L is a characteristic size of the system. This contribution can be the same order of magnitude as the first, McVittie-Sandage term, and so is not obviously negligible when talking about active galactic nuclei as sources, for example. It is crucial to realize that this should not be interpreted statistically, i.e. averaging over sources in low density and high density regions, but treated for an individual line of sight. Similarly it should not be treated as though the source was in the linear density perturbation regime.

Methods exist for ameliorating these systematics, e.g. observing several well separated sources. However the precision required for measurement of redshift drift at a signal-to-noise of merely unity is $dz \approx 10^{-10}$ over a year (or 10^{-9} over 10 years), while a 1% measurement of the dark energy equation of state (assumed constant) requires $dz \approx 10^{-13}$ over a year. Systematics would need to be reduced below these levels.

To see how far we can beat down these challenges we first explore the cosmological sensitivity

of the probe, then in the next two sections consider some theoretical and experimental leverages.

Figure 1 shows the sensitivity of the drift \dot{z} as a function of source redshift to the cosmological parameters of the matter density Ω_m and dark energy equation of state $w(a) = w_0 + w_a(1 - a)$ where w_0 is its present value and w_a a measure of its time variation. The key properties to notice are: 1) The sensitivity curves are different shapes, indicating no strong covariance between the effects of the different parameters, 2) The greatest sensitivity is to the matter density, and this continues to outweigh the equation of state parameters at higher redshifts, by ever increasing factors, and 3) The initial rise of the equation of state sensitivities is sharp, achieving 50% of the maximum sensitivity at quite low redshifts. These characteristics suggest that low redshift measurements, especially if they have better signal to noise than higher redshift ones, could be valuable for cosmological leverage on dark energy through the redshift drift probe. We will see that this in fact fits in well with the new experimental techniques introduced in Sec. 4.

At low redshift $\dot{z} \approx -H_0 q_0 z$ so the cosmological sensitivity initially increases linearly with redshift. If the precision is photon noise limited, then it will go inversely with the luminosity distance. Since luminosity distance grows initially linearly with redshift, then more quickly at higher redshift, this indicates that low redshift may give the strongest cosmological leverage.

Another consideration is that the low redshift q_0 dependence (which accords with redshift drift being a direct probe of acceleration) implies the sensitivity to Ω_m will be a factor $\sim 3/2$ better than to w_0 , in agreement with Fig. 1. The sensitivity to matter density continues to increase with redshift, growing from linear with z to proportional to $z^{3/2}$ at high redshift, swamping the dark energy parameters, whose sensitivities decline at high redshift. These characteristics give merit to further exploration of the use of low redshift sources.

Figure 2 considers measurements at low, medium, and high redshift ranges and compares the precisions needed on \dot{z} to give roughly comparable constraints on dark energy equation of state parameters. **More discussion once I've made the plot.**

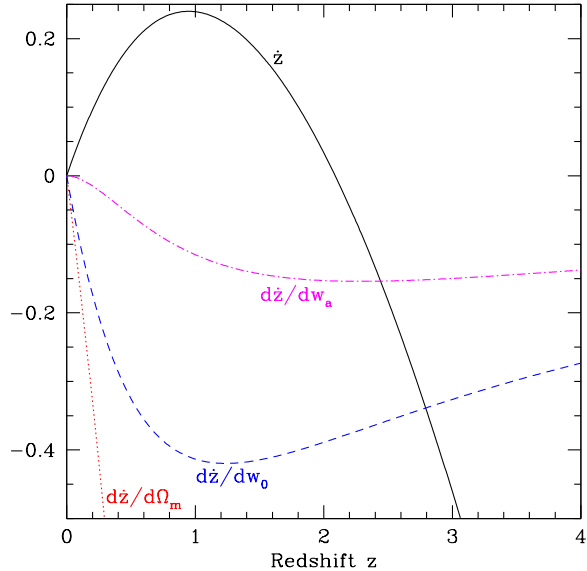


Fig. 1.— The dependence of the redshift drift \dot{z} and the sensitivities $\partial\dot{z}/\partial p$ to various cosmological parameters p are shown as functions of redshift. All quantities are in units of H_0 , hence the redshift drift over an observing time Δt is $\Delta z \lesssim H_0 \Delta t = 10^{10} h(\Delta t/\text{yr})$.

Fig. 2.— Joint constraints on the dark energy equation of state parameters w_0 and w_a are shown at 68% confidence level. Note that for comparable constraints, less stringent accuracy is needed when using low redshift sources. **Try Fisher contours for measurements over [0.1,0.5], [0.7,1.2], [2.5,3]**

3. Theoretical Ideas

Since the requirements of measuring dz are so challenging, theoretical concepts for observational probes that inherently use long time scales or multiple measurements in one system would be of particular interest. A long lever arm in time and many measurements could reduce the requirements on individual measurement precision. The universe itself provides sources at many different epochs, spread out over a Hubble time. Likewise, individual sources can provide many different signals, e.g. spectral lines or wavetrains. In this section we explore the use of each of these characteristics, and then their combination, in potential probes of acceleration.

3.1. Many sources: Radial baryon acoustic oscillations

While the light from sources at different redshifts reaches us after being emitted at vastly different times, this does not inform us regarding redshift drift since that involves the change of a given source over time. However, we can think of a statistical ensemble of objects collectively as a source, for example defining a baryon acoustic feature in the density power spectrum. This encodes a particular comoving scale, roughly the sound horizon s at baryon-photon decoupling. By measuring it along the line of sight, we are measuring a cosmic length $dr \sim 150$ Mpc with endpoints at two different redshifts so $dr = dz/H$. Since $dz \approx 0.05$ then H is fairly constant over this interval and we can simply say we obtain a measurement $H(z_1)$, where z_1 is the mean redshift. This is called a radial baryon acoustic oscillation (BAO) measurement, of the quantity sH .

Carrying this out in a second redshift slice delivers $H(z_2)$. Propagating the errors from each we can create a differential radial BAO (drBAO) measurement

$$R = s(H_2 - H_1) . \quad (6)$$

For redshift differences not small compared to unity, we measure the Hubble expansion parameter at times separated by a substantial fraction of the Hubble time, $\sim 10^{10}$ y. That is, we have left it to the universe to do the work of providing the long time baseline.

While drBAO gives the “Hubble drift” rather than the redshift drift, these two quantities are closely related, and indeed the Hubble drift measurement has some useful differences as shown in Table 1. The nuisance parameter for comparing to cosmology theory is H_0 for the redshift drift, while it is the much better known sound horizon s for drBAO. While redshift drift has a null at the acceleration-deceleration transition, drBAO has a null at the superacceleration or phantom transition, when the total equation of state of the universe $w_{\text{tot}} = -1$. Finally, spectroscopic galaxy surveys measuring BAO also provide drBAO so no separate instrument or experiment is required.

Probe	Quantity	Nuisance	Sign
z drift	$(1+z)H_0 - H(z)$	H_0	$w_{\text{tot}} < -1/3$
drBAO	$s[H(z_2) - H(z_1)]$	s	$w_{\text{tot}} < -1$

Table 1: Redshift drift and differential radial BAO both directly measure the acceleration of the universe, but with different nuisance parameters and observational requirements.

3.2. Many signals: Cosmic pulsars

The long time baseline of the drBAO probe ameliorates the redshift precision needed, to simply that needed to measure the radial BAO scale ($dz \approx 10^{-3}$). However it does involve the clustering of large scale structure and a statistical measure rather than simply photon propagation from an individual source. If a single source gave many measurements, i.e. emitted many signals each of which could be used to measure redshift drift, then the requirement on the redshift precision can also be ameliorated in this manner. Conventionally this is thought of in terms of many spectral lines; we return to this later but here explore the time domain.

If the source repeatedly emitted signals, then by measuring N of them we could hope to statistically reduce the uncertainty on the redshift drift. Moreover, if there is a specific pattern to the signals, e.g. a periodicity, then further gains can be made. This is the idea behind the period probe, or cosmic pulsar test; here we follow the textbook treatment of ?. The time observed for the arrival

of the N th pulse with emitted period P is

$$\begin{aligned}
t_N &\equiv t_o(NP) \\
&= NP \frac{dt_o}{dt_e} + \frac{1}{2} (NP)^2 \frac{d^2 t_o}{dt_e^2} + \dots \quad (7) \\
&= NP(1+z) \\
&\quad + \frac{1}{2} (NP)^2 (1+z) [(1+z) H_0 - H(z)] \quad (8)
\end{aligned}$$

The redshift drift (in square brackets) is thus enhanced by N^2 and can be specifically fit to the quadratic behavior of the time series, helping to make a clean detection. There is an extensive literature on pulsar timing and efficient fitting of different contributions ?.

While pulsars are fantastically regular clocks, well suited to this probe, we do not currently detect them at cosmological distances in the Hubble flow (but see ?). The idea behind cosmic pulsars is not restrict to neutron stars, however. One could consider other sources of (quasi-)periodic signals such as gravitational waves from super-massive binary black hole inspirals, which should be detectable at cosmic distances. An issue here (other than detecting such sources) is that in these systems redshift is not measured separately but is tied into the chirp mass combination with the black hole masses. Any evolution in the black hole masses – or Newton’s constant – would be a systematic; see the analysis in Appendix B of ? following a suggestion by Linder. Finally, any other accelerations, such as the motion of the system through an inhomogeneous gravitational potential or pulsar or gravitational wave kicks, would be a systematic.

3.3. Multiple sources and signals: Strongly lensed quasars

The ideal situation would be to combine the long time baseline provided by cosmological distances as in the drBAO method with the multiple signals per source as in the cosmic pulsar method. While this cannot be exactly done, some of advantages of each enter in the use of strongly lensed sources, plus the ability to do a differential rather than absolute measurement.

Strong gravitational lensing produces multiple images of the source, and so in a single system one can measure the redshift along multiple lines of sight. Gravitational lensing itself is achromatic

in the geometric optics regime (wavelength divided by effective lens scale much less than one, an excellent approximation at ultraviolet and optical wavelengths) and so the redshifts will be the same. If the propagating light is absorbed in the Lyman alpha forest due to neutral hydrogen gas along the path, then many narrow spectral features arise, enabling multiple measurements of the redshift drift.

Moreover, due to the different light paths there will be time delays between the spectra observed of each image. This is used in strong lensing as a cosmological distance probe itself (see, e.g., ? and references therein). Here, however, it provides a time baseline for the redshift drift of the individual source. If the time delay were of order 10 years (or even better a substantial fraction of the Hubble time) then the required redshift measurement precision would be eased, but observed systems have time delays of days to a year. Still, the universe is giving us for free a time baseline of a year though the redshift observations may be done in a single night.

Note that unlike for time delay distances we have no need to model the time delay through knowledge of the lens mass profile, image geometry, etc. – all we need to do is measure it from monitoring the light curves of the images. A bright, time varying source such as a quasar is ideal for this, and the time delay is measured from the photometric light curves (see, e.g. ?? for statistical techniques for robust estimation). The Lyman alpha spectral features do not enter in this part. Since we do not need to model the lens mass profile, we can use cluster lenses, with larger time delays, rather than restricting to galaxy lenses as for the time delay distance technique.

If the lines of sight are sufficiently close together, then they can be observed simultaneously, allowing a direct differential measurement to give the redshift drift, rather than an absolute one. Furthermore, this increases the likelihood that the Lyman alpha absorption is coherent between the multiple lines of sight. The transverse distance at redshift z between lines of sight separated by angle $\Delta\theta$ is

$$\Delta r = D_A \Delta\theta \approx 6 \left(\frac{H_0 D_A}{0.4} \right) \left(\frac{\Delta\theta}{1''} \right) h^{-1} \text{kpc} . \quad (9)$$

Note that for $z = 1 - 3.5$, $H_0 D_A$ is almost con-

stant at 0.4 in a cosmology near the concordance model. Image separations tend to be in the 1–5'' range. For such transverse separations, much smaller than the gas Jeans scale of $\sim 300 h^{-1}$ kpc, the Lyman alpha lines should be coherent in the multiple images ?. Note that if we wanted to use very long time delay systems (though few are known, none with $\Delta t > 3$ y) then these tend to have larger image separations, roughly $\Delta t \sim (\Delta\theta)^2$ and the coherence may be degraded for hypothetical systems with separations greater than tens of arcseconds.

Wide field surveys such as Dark Energy Survey and LSST will find approximately 10^3 and 10^4 strongly lensed quasars, respectively. Monitoring campaigns such as COSMOGRAIL ? and STRIDES ? obtain long term light curves for their images, measuring the time delays. Depending on the time delay, photometry quality, and other factors it may take up to 1000 nights to obtain a time delay estimation, though note that the accuracy requirements may be relaxed from the time delay distance case, e.g. 5% accuracy may be sufficient for this not to contribute significantly to the redshift drift uncertainty. The differential redshift measurement itself takes only a single night, so the story of the universe may be revealed in 1000 nights and a night ?.

Lensing can affect the image redshifts if the lens is moving ??. From Eq. (3) we see this arises because the dot product between the photon four-momentum and the source and observer four-velocities has to go through the intermediate step of the lens plane, where the deflection shifts the angle between the vectors. The redshift contribution is of order $v\delta\alpha$, where $\delta\alpha \sim \psi$ is the deflection angle. The redshift drift contribution is then $(v\delta\alpha)'$, much smaller than a standard peculiar acceleration of the source and so can be neglected.

Embedded within the image spectra are not only the source redshift, but the redshifts of each Lyman alpha absorber. Thus in a single night we get not only multiple images with cosmology-provided time delays, but multiple signals within each image spectrum. The $N_{\text{line,q}}$ spectral lines in the quasar, perhaps $\mathcal{O}(10^3)$, help to improve the signal-to-noise by $\sqrt{N_{\text{line,q}}}$ but moreover the $N_{\text{line,f}}$ lines in the forest, also perhaps $\mathcal{O}(10^3)$, simultaneously applies the redshift drift test at

multiple redshifts (with their individual $\dot{z}(z)$), potentially improving the cosmological model constraints. We discuss this further in the next section.

4. Experimental Approaches

In this section we turn from theoretical speculation to consideration of innovative experimental approaches, with practical details on how to obtain highly precise redshift measurements, especially through differential observations.

[EL: Fit this next paragraph in somewhere?]

First, a simultaneous differential measurement between time delayed spectra is more robust than individual absolute measurements of redshift. Traditionally, one might wavelength calibrate the spectra with an external standard, such as an iodine cell, and then repeat this one or ten years later with the next redshift measurement of the source. However, the wavelength calibration is not guaranteed to remain fixed over this long time span; indeed ? find it can shift significantly over a single night with changes in temperature, humidity, etc. These stability issues are removed with a simultaneous differential measurement.

[EL: Make transition to this text and following subsections.]

This is over an order of magnitude improvement of the high-precision redshift measurement of $\sigma_z = 6 \times 10^{-7}$ obtained from the radio absorption line in 3C 286 at $z = 0.849$ (?).

5. [OII] and [OIII] Emission Line Galaxies as Targets

Emission line galaxies are excellent candidates for the measurement of precision redshifts. The unique signature of doublets amidst other emission lines allows unambiguous identification of the [OII] $\lambda\lambda 3727\text{--}3729\text{\AA}$ and [OIII] $\lambda\lambda 4959\text{--}5007\text{\AA}$ doublets. Their high line fluxes provide strong signals that suppress statistical Poisson uncertainty. Doublets occupy only a narrow bandwidth that spectrographs must span. The two lines of a doublet are produced by the same atoms and therefore share a common line profile: as the wavelength separation of the two lines is proportional to $(1+z)$, their cross-correlation in log-wavelength provides a measure of redshift that is independent of the

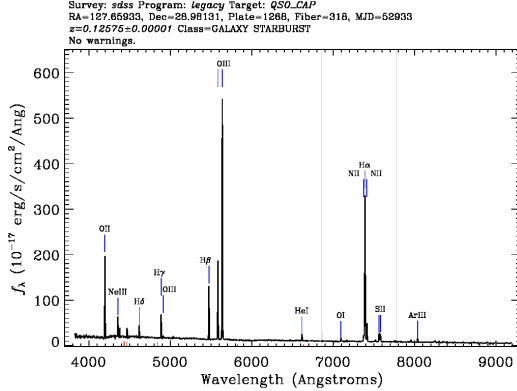


Fig. 3.— Spectrum of SDSS target specified by Plate #1268, Fiber #318 from the SDSS3 DR10.

specific shape of the line profile.

Potential targets are selected from the Sloan Digital Sky Survey data release SDSS3 DR10. The Portsmouth Emission-Line Kinematics table (?) is used to select objects with $z > 0.08$ and sharp and bright [OII] and/or [OIII] emission lines. The redshifts, velocity dispersions Δv , line strengths, and host continuum levels for a select set of galaxies are shown in Table 2. The two-line average Δv for [OII], and the continua flux for about doublets are given. Although we use its velocity dispersions, the Portsmouth table gives “rest-frame” fluxes corrected for dust correction; the observed fluxes needed to simulate observations are taken from the spZline data model (?). In some cases only one doublet is visible, for example with high-redshift galaxies where [OIII] features are shifted to the near-infrared and are difficult to access from ground-based observations. A representative target, from Plate #1268, Fiber #318, has its SDSS spectrum shown in Figure 3.

The tabulated galaxies are not the product of an exhaustive search and are meant to represent a minimum of what can be available as good candidates targets. Future surveys such as eBOSS, Dark Energy Spectroscopic Instrument, and Euclid will specifically target emission-line galaxies from which the best targets can be identified. In the scenarios considered in this article, redshift precision scales with the inverse of line width and the inverse square root of line flux.

The spectral regions of interest are around each doublet. In the calculations that follow, these areas are modeled as a function of wavenumber σ as

$$B(\sigma) = \frac{a_1}{\sqrt{2\pi s_1^2}} \exp \left[-\frac{(\sigma - \sigma_1)^2}{2s_1^2} \right] + \frac{a_2}{\sqrt{2\pi s_2^2}} \exp \left[-\frac{(\sigma - \sigma_2)^2}{2s_2^2} \right]. \quad (10)$$

The two lines have central wavenumbers σ_1 and σ_2 , and share a common Gaussian profile with width parameterized by velocity dispersion such that $s_i = \sigma_i \Delta v / c$.

6. Spectrographs Considered For Redshift Measurements

The precision with which redshift can be determined depends on the instrument used for the measurement. We consider several spectrometers designs, including a “Conventional” high-resolution dispersion spectrograph and the interferometric instruments “EDI”, “SHS”, and “ED-SHS”. Interferometers produce a Fourier transform of a signal, converting sharp spectral features into a wave patterns whose frequency is dependent on the feature wavelength. Interferometers provide increased statistical sensitivity to wavelength measurements and potentially have less sensitivity to systematic uncertainties.

Some common assumptions are made for the spectrometers. The baseline observation is for an 8-hour exposure on a 10-m telescope. To allow direct comparison of the designs, all systems are assigned the same total throughput of 70%. The dispersion spectrometer used for Conventional, EDI, and ED-SHS instruments has $R = 20000$ with point-spread-function dominated by the pixel top-hat function. For all cases considered photon noise dominates uncertainties, nevertheless we include a detector read noise of $2e^-$, total integrations split into 2-hour exposures, and a dark current of $2e^- s^{-1}$. Blocking filters remove flux in wavelengths outside the regions of interest. The new moon CTIO sky emission is included and is small compared to the galaxy continuum. Spatial information is unimportant and the target is considered as point-like: a circular aperture of $1''$ diameter is assumed to cover the full line flux. The effective PSF (including pixels and possible sub-pixel quantum efficiency variation) Nyquist samples the intrinsic line profiles. When appropriate,

TABLE 2
TARGET LINE PROPERTIES.

Plate	Fiber	z	Doublet	Δv (km s ⁻¹)	Flux 1 (erg s ⁻¹ cm ⁻²)	Flux 2 (erg s ⁻¹ cm ⁻²)	Continuum (erg s ⁻¹ cm ⁻² Å ⁻¹)
1523	602	0.089	[OIII]	5.14	7.04×10^{-16}	2.13×10^{-15}	1.97×10^{-17}
1935	204	0.098	[OII]	10.054	1.06×10^{-14}	1.28×10^{-14}	2.39×10^{-16}
			[OIII]	10.04	1.96×10^{-14}	5.93×10^{-14}	1.92×10^{-16}
1036	584	0.108	[OIII]	4.55	3.47×10^{-16}	1.05×10^{-15}	4.42×10^{-17}
2959	354	0.120	[OIII]	6.86	1.11×10^{-16}	3.36×10^{-16}	1.51×10^{-18}
1268	318	0.126	[OII]	10.044	5.89×10^{-15}	6.29×10^{-15}	1.77×10^{-16}
			[OIII]	10.04	1.09×10^{-14}	3.32×10^{-14}	1.46×10^{-16}
1657	483	0.221	[OII]	10.359	4.69×10^{-15}	4.28×10^{-15}	1.36×10^{-16}
			[OIII]	10.30	6.07×10^{-15}	1.84×10^{-14}	1.09×10^{-16}
1073	225	0.272	[OII]	84.746	8.38×10^{-16}	1.05×10^{-15}	3.36×10^{-17}
			[OIII]	1.43	3.75×10^{-16}	1.14×10^{-15}	3.89×10^{-17}
1514	137	0.318	[OII]	10.005	1.20×10^{-15}	1.74×10^{-15}	6.35×10^{-17}
			[OIII]	10.01	3.85×10^{-16}	1.17×10^{-15}	1.07×10^{-16}
4794	757	0.560	[OII]	45.890	2.03×10^{-16}	3.18×10^{-16}	8.18×10^{-18}
			[OIII]	26.45	8.29×10^{-17}	2.51×10^{-16}	1.51×10^{-17}
1059	564	0.693	[OII]	9.580	1.40×10^{-17}	1.94×10^{-14}	1.47×10^{-17}

the sampling along the spatial axis is not included explicitly in the signal equations for conciseness.

Projected redshift precisions are calculated with Fisher matrix analysis with the source redshift z as the only free parameter. Precisions scale as the inverse square root of exposure time and inverse of telescope aperture. For the SHS and when the $R = 20000$ spectrographs resolve the spectral line, the precision scales inversely with the line dispersion velocity. As the measurements are source-noise dominated, redshift precisions scale as the inverse square of line flux.

We are interested in uncertainties in redshift drift. This is in some ways simpler than measuring absolute redshifts because correlated redshift uncertainties cancel each other when measuring drift. Instruments contribute sources of measurement uncertainty in redshift drift: through limitations in the calibration of wavelength, uncertainty in the conversion from pixel counts to physical flux, and uncertainty in the point spread function. Each spectrograph type has different susceptibilities to systematic uncertainties.

6.1. Conventional Dispersion Spectrograph

The redshift of a galaxy can be measured from the output of a dispersion spectrograph, such as shown in Figure 3. For an input spectrum $B(\sigma)$ the expected signal is

$$I(\sigma) = [B(\sigma) \otimes \text{PSF}(\sigma)] \text{III} \left(\frac{\sigma}{p} \right), \quad (11)$$

where p is the spacing of the wavenumber sampling and the Shah function III is the set of delta functions that specify the discrete sampling,

The wavelengths of the observed lines are compared to the corresponding known restframe to give the redshift. **Looking into uncertainty of the double wavelengths. The [OII] double wavelengths are known to 0.0010Å (?).** Projected statistical uncertainties from an $R = 20000$ spectrograph for the target galaxies are given under the “Conventional” column of Table 3. Results from [OII], [OIII], and their combination are listed separately.

Not included in Table 3 are sources of instrumental systematics. Wavelength calibration is performed through observations of arc lamps emitting lines at known wavelengths. The line density

TABLE 3
STATISTICAL UNCERTAINTIES OF SELECT SDSS TARGETS WITH AN 8 HOUR EXPOSURE ON A 10-M
TELESCOPE FOR DIFFERENT SPECTROGRAPHS.

Plate	Fiber	Doublet	Conventional	EDI	SHS	ED-SHS
1523	602	OII	1.7×10^{-8}	5.8×10^{-9}	2.4×10^{-8}	5.9×10^{-9}
1935	204	OII	1.4×10^{-8}	4.4×10^{-9}	1.7×10^{-8}	4.5×10^{-9}
		OIII	6.3×10^{-9}	2.1×10^{-9}	7.9×10^{-9}	2.0×10^{-9}
		OII&OIII	5.7×10^{-9}	1.9×10^{-9}	7.2×10^{-9}	1.9×10^{-9}
1036	584	OIII	2.3×10^{-8}	8.8×10^{-9}	4.2×10^{-8}	7.8×10^{-9}
2959	354	OIII	6.0×10^{-8}	2.0×10^{-8}	9.5×10^{-8}	2.1×10^{-8}
1268	318	OII	1.9×10^{-8}	5.7×10^{-9}	2.5×10^{-8}	6.4×10^{-9}
		OIII	8.6×10^{-9}	2.7×10^{-9}	1.1×10^{-8}	2.8×10^{-9}
		OII&OIII	7.9×10^{-9}	2.4×10^{-9}	1.0×10^{-8}	2.5×10^{-9}
1657	483	OII	2.4×10^{-8}	7.1×10^{-9}	3.1×10^{-8}	8.0×10^{-9}
		OIII	1.2×10^{-8}	3.9×10^{-9}	1.6×10^{-8}	4.0×10^{-9}
		OII&OIII	1.1×10^{-8}	3.4×10^{-9}	1.4×10^{-8}	3.6×10^{-9}
1073	225	OII	7.2×10^{-7}	2.2×10^{-7}	8.7×10^{-7}	2.3×10^{-7}
		OIII	1.2×10^{-8}	6.2×10^{-9}	1.3×10^{-8}	5.1×10^{-9}
		OII&OIII	1.2×10^{-8}	6.2×10^{-9}	1.3×10^{-8}	5.1×10^{-9}
1514	137	OII	4.3×10^{-8}	1.4×10^{-8}	5.5×10^{-8}	1.4×10^{-8}
		OIII	5.6×10^{-8}	1.6×10^{-8}	1.3×10^{-7}	1.8×10^{-8}
		OII&OIII	3.4×10^{-8}	1.0×10^{-8}	5.1×10^{-8}	1.1×10^{-8}
4794	757	OII	6.2×10^{-7}	1.9×10^{-7}	6.6×10^{-7}	2.0×10^{-7}
		OIII	4.1×10^{-7}	1.3×10^{-7}	9.0×10^{-7}	1.3×10^{-7}
		OII&OIII	3.4×10^{-7}	1.1×10^{-7}	5.3×10^{-7}	1.1×10^{-7}
1059	564	OII	1.7×10^{-8}	5.5×10^{-9}	1.6×10^{-8}	5.6×10^{-9}

is sparse, in that an arc line is not placed on every detector pixel. If the arc is taken simultaneously with the science exposure, a minimum wavelength interpolation distance must be maintained so that the arc does not interfere with the doublet. Otherwise, the arc must be observed in a different exposure. Therefore, temporal and/or wavelength interpolation are applied to calibrate wavelengths.

The small number of pixels measuring line flux places stringent requirements on flatfield calibration. The FWHM of a 10 km s^{-1} feature is spanned by 3.15 pixels along the dispersion axis, and (for our calculations) 3 pixels along the spatial axis. A single pixel covered by one of the [OIII] lines of the SDSS target specified by Plate #1268, Fiber #318 has $\sim 10^6$ counts; in order for photon noise to dominate over pixel flux uncertainty the calibration must be done to significantly better than 0.1%.

Uncertainty in the often variable and charge-dependent point spread function can bias the determination of the line centroids. Just as with the flux calibration requirement, sub-per-mil accuracy in predicted pixel counts is required. For redshift drift, these calibration requirements are differential between observations taken over the duration of the survey: if absolute calibration is not achieved, instrumental stability is essential.

6.2. Externally Dispersed Interferometer

The Externally Dispersed Interferometer (EDI; ?) is a candidate instrument with which to measure precision redshifts. An EDI is the sequence of a Fourier transform spectrograph (FTS) and a dispersion spectrograph. The FTS is an interferometer that shifts the phase of incoming coherent light by an amount dependent on wavelength and a delay between the two arm lengths. The ensuing dispersion spectrograph takes the phased light and separates it into fine wavelength bins. For an individual wavelength bin the output signal depends on the phase introduced by the interferometer; multiple measurements taken after adjusting the delay make apparent a modulation in the output signals. Therefore, in an EDI the wavelength can be measured using both the calibration methods of a standard dispersion spectrograph *and* from the modulations of signal apparent when changing the FTS arm-lengths. As a consequence, it was shown by ? that EDI's provide line-velocity

measurements that are more precise than with a dispersion spectrograph.

An EDI produces measurements that can be related to a conventional spectrum

$$I(\sigma) = B(\sigma) \otimes \text{PSF}(\sigma), \quad (12)$$

and an independently measurable whirl

$$W(\sigma) = \frac{1}{2} [e^{i2\pi\tau_d\sigma} B(\sigma)] \otimes \text{PSF}(\sigma), \quad (13)$$

where B is the input spectrum, τ_d is the interferometer delay, and PSF is the blurring response of a pure frequency.

The heterodyning feature of the EDI is seen in the Fourier transforms of the above expressions:

$$i(\rho) = b(\rho) \text{psf}(\rho) \quad (14)$$

$$w(\rho - \tau) = \frac{1}{2} b(\rho) \text{psf}(\rho - \tau). \quad (15)$$

The EDI whirl has the instrumental frequency response shifted into a new ρ range to allow spectral resolution on scales tuned by the choice of τ . In the calculations that follow, the delay is chosen to resolve the FWHM of the line with lower wavenumber, $\tau = (2.36s_1)^{-1}$.

An EDI observation is actually a series of measurements

$$I(\sigma)_{\Delta\tau} = [B(\sigma) (1 + \cos(2\pi(\tau + \Delta\tau)\sigma + \phi_y)) \otimes \text{PSF}(\sigma)] \text{III} \left(\frac{\sigma}{p} \right), \quad (16)$$

where p is the spacing of the wavenumber sampling, ϕ_y is the initial phase, and $\Delta\tau$ represents the changes in time delay in the series of exposures; for our calculations we choose $\Delta\tau = (1 + 0.25n)\tau$ with $n \in \{0, 1, 2, 3\}$ with the change achieved by adjusting an interferometer arm length. The first term represents the signal obtained with a conventional spectrograph while the second cosine term introduces a wavelength-dependent phase that provides additional leverage in measuring redshift.

The expected signal for one of the [OIII] lines of the SDSS target specified by Plate #1268, Fiber #318 is shown in Figure 4. In this case the nominal delay is $\tau = 3.57 \text{ mm}$ with measurements made in steps of 0.892 mm .

The redshift precisions on the target galaxies are given in Table 3, where each of the four phases receives a 2-hour exposure. The EDI performance

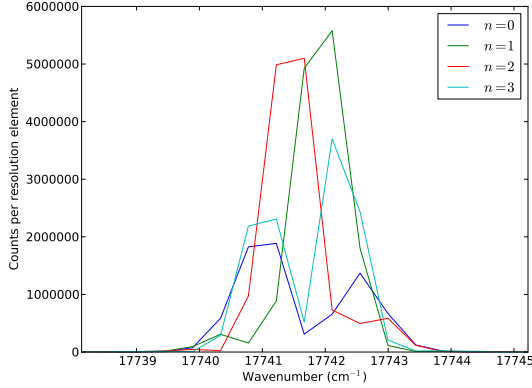


Fig. 4.— The expected EDI signal from the four phase measurements for one of the [OIII] lines of the SDSS target specified by Plate #1268, Fiber #318. The four phases parameterized by n is defined in Eqn. 16.

includes that of the Conventional spectrograph plus the additional contribution from the whirl; in total the EDI outperforms the Conventional spectrograph in redshift precision by a factor of ~ 3 .

Separating the EDI information into Conventional and whirl contributions, the signal and constraint from the Conventional spectrograph contribution shares those same systematic uncertainties. The whirl component is best calibrated using arc lamps in the science exposure. The arc lines determine the configuration of the EDI itself, ϕ_y and the $\Delta\tau$'s, and do not have to be close to the science lines. This avoids the temporal and wavelength interpolation needed in conventional spectrographs. Wavelength uncertainty would then come from mismeasurement of phase and frequency due to pixels local to the science lines. Absolute flux and PSF uncertainties then become irrelevant.

Flux miscalibration still affect the line profiles, resulting in potential bias in effect wavelength similar to the Conventional case in scale. PSF calibration is facilitated with the presence of arc lines from which the PSF can be directly determined.

6.3. Spatial Heterodyne Spectroscopy

6.3.1. Measuring Redshift

Redshift can also be measured through the sum and the difference of observed wavenumbers of two lines whose restframe wavenumbers are known:

$$(1+z) = \frac{\sigma_{10} + \sigma_{20}}{\sigma_1 + \sigma_2} = \frac{\sigma_{10} - \sigma_{20}}{\sigma_1 - \sigma_2}, \quad (17)$$

where σ_i is the observed and σ_{i0} the restframe wavenumber of line i . At face value, the measurement of $\sigma_1 \pm \sigma_2$ should be expected to suffer larger uncertainty than that of the wavenumber of a single line. To counter this expectation, we consider a scenario where the experimental setup has an output that is naturally sensitive to $\sigma_1 \pm \sigma_2$. The differential measurement can be immune to certain systematic uncertainties encountered when using dispersion spectrographs. Redshifts are measured from the relative shift of a single line profile common to two lines of a doublet with no PSF blurring of the line profiles.

6.3.2. Signal

We consider Spatial heterodyne spectroscopy (SHS) (?) as a means to get a direct measurement of $\sigma_1 \pm \sigma_2$. Conceptually, the SHS can be understood as an interferometer with the mirrors replaced by diffraction gratings. (Practically we assume an interferometer configuration that avoids the 50% light loss inherent to Michelson interferometers.) The gratings have line-spacing d and both are tilted by θ with respect to the optical axis. The deflected light from each grating exits the interferometer as a plane wave propagating with angle γ away from the optical axis, given by the grating equation

$$\sigma (\sin \theta + \sin (\theta - \gamma)) = m/d, \quad (18)$$

where σ is the wavenumber and m the diffraction order. The angle of the emergent wave can be re-expressed as

$$\sin \gamma = -\cos \theta \left(\frac{m}{d\sigma} - \sin \theta \right) + \sin \theta \sqrt{1 - \left(\frac{m}{d\sigma} - \sin \theta \right)^2}, \quad (19)$$

which is useful in calculations.

The two wavefronts from the two gratings, incident on the detector at angles $-\gamma$ and γ , interfere

to make a fringe pattern with frequency

$$f_x = 2\sigma \sin \gamma. \quad (20)$$

For an input spectrum of $B(\sigma)$, the intensity seen at the detector at position x is

$$I(x) = \frac{1}{\Delta x} \left[\int_0^\infty B(\sigma) (1 + \cos(2\pi x(2\sigma \sin \gamma))) d\sigma \otimes \text{PSF}\left(\frac{x}{p}\right) \right] \quad (21)$$

where p is the spacing of the wavenumber sampling, and for simplicity we assume a square collimated beam that covers a range $\Delta x \gg (2\sigma \sin \gamma)^{-1}$. The Littrow wavenumber σ_0 is defined such that $2\sigma_0 \sin \theta = m/d$, $\gamma = 0$ and no fringe patterns are produced.

6.3.3. Toy Example

For illustration, consider a toy example where the input signal consists of two δ -functions with the same intensity

$$B(\sigma) = \delta(\sigma_1) + \delta(\sigma_2). \quad (22)$$

The output signal density in this case is

$$\begin{aligned} I(x) &= \frac{1}{\Delta x} [2 + \cos(2\pi(2\sigma_1 \sin \gamma_1)x) + \cos(2\pi(2\sigma_2 \sin \gamma_2)x)] \\ &= \frac{2}{\Delta x} [1 + \cos(2\pi(\sigma_1 \sin \gamma_1 + \sigma_2 \sin \gamma_2)x) \times \cos(2\pi(\sigma_1 \sin \gamma_1 - \sigma_2 \sin \gamma_2)x)]. \end{aligned} \quad (23)$$

The two mixing of the sinusoidal outputs of the two lines results in two beat frequencies $(\sigma_1 \sin \gamma_1 \pm \sigma_2 \sin \gamma_2)$.

When the SHS is configured such that the Littrow wavenumber is very close to σ_1 and σ_2 (and hence γ_1 and γ_2 are small),

$$\sigma_{1,2} \sin \gamma_{1,2} \approx 2(\sigma_{1,2} - \sigma_0) \tan \theta \quad (25)$$

and the beat frequencies can be expressed as $2(\sigma_1 + \sigma_2 - 2\sigma_0) \tan \theta$ and $2(\sigma_1 - \sigma_2) \tan \theta$. Each beat frequency provides information on either $\sigma_1 \pm \sigma_2$, the two quantities that directly lead to redshift.

The ratio n between the beat frequencies can be chosen by adjusting the SHS configuration to give

$$\sigma_0 = \frac{\sigma_1 + \sigma_2}{2} - \frac{\sigma_1 - \sigma_2}{2n}. \quad (26)$$

For $n = \infty$ the Littrow wavenumber is set to the average of the two lines: $\sigma_0 = (\sigma_1 + \sigma_2)/2$ and the first beat frequency is zero, which in practice is difficult to quantify through measurement. When $n = 1$ the Littrow wavenumber is σ_2 , meaning that line produces a flat signal and the other is the source of the oscillations; the value of the two beat frequencies are equal.

6.3.4. Performance on Target Galaxies

We calculate the expected signal using the first order $m = 1$ for a SHS with grating line density $1/d = 1200 \text{ mm}^{-1}$ and using the more realistic double line model of Eq. 10. Different configurations of the SHS are achieved by adjusting the grating tilt angle θ , although swapping gratings can achieve a similar effect. The SHS configuration can then be expressed in terms of the Littrow wavenumber.

For the [OIII] doublet of the SDSS target specified by Plate #1268, Fiber #318 the condition for having only one beat frequency occurs when $\sigma_0 = \sigma_2 = 17913 \text{ cm}^{-1}$ and occurs at $\theta = 0.341551$. Different choices of Littrow wavenumber produce different output signals: Figure 5 shows the expected counts adjusting σ_0 to produce beat frequency ratios $n = 1/3.5, 1/1.05, 1, 1.05, 3.5$ according to Eq. 26. The maximum x is chosen to be $(12s_1 \tan \theta)^{-1}$ in order to cover the decay caused by the line-width. The effect on the signal of the choice of the beat frequency of $2(\sigma_1 + \sigma_2 - 2\sigma_0) \tan \theta$ relative to the $2(\sigma_1 - \sigma_2) \tan \theta$ frequency is clearly apparent. The precision is insensitive to the choice of σ_0 , except for small deviations near $n = 1$ and at integer ratios of the beat frequencies; we choose the case of $n = 1.5$ or $\theta = 0.3421194$ (a change in angle of $1.95'$ from the $n = 1$ case) as a representative example where the pixels resolve the frequencies of interest.

The redshift precisions on the target galaxies are given in Table 3. The statistical uncertainties are slightly worse than for the Conventional spectrograph and well below EDI. However, the results have reduced sensitivity to PSF uncertainties.

Wavelength calibration is tied to the determination of the EDI system parameters, the grating density $1/d$ and angle θ . Both can be calibrated externally through direct measurements, or arc lamp exposures; including lamp light in sci-

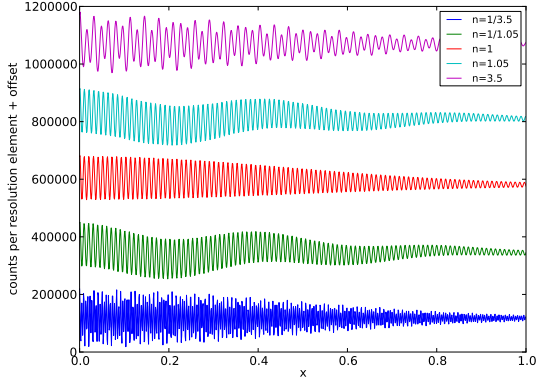


Fig. 5.— The output signal for positive x of the SHS configurations that give the four different Littrow numbers according to $n = 1/3.5, 1/1.05, 1, 1.05, 3.5$ in Equation 26. Only half the signal is shown: it is symmetric about $x = 0$.

ence exposures is not preferred as all sources of light contribute the noise background. Alternatively the long exposures can be divided into sub-exposures each with a different SHS configuration, either by changing the gratings or by rotating the grating angles by a series of $\delta\theta$. The data themselves can be then used to fit for the hardware parameters.

The line signal is distributed over thousands of pixels reducing the pixel flux requirement to better than 1%, much less stringent than for the the Conventional and EDI spectrographs.

Converting the spectrum to Fourier space transforms the sharp imperfectly-known line profiles into the low-frequency envelope, distinct from the high-frequency wiggles characteristic to each configuration that inform the redshift measurement. The PSF blurring applies not in wavenumber space where it affects line shapes but rather in physical space after the conversion of the lines into cosine functions; the PSF does not directly bias the effective wavelength of lines.

6.4. ED-SHS

The two doublet lines combine to produce a mixed signal in an SHS. Sending SHS light, such as those signals shown in Figure 5, into an ensuing dispersion grating allows the disentangling of

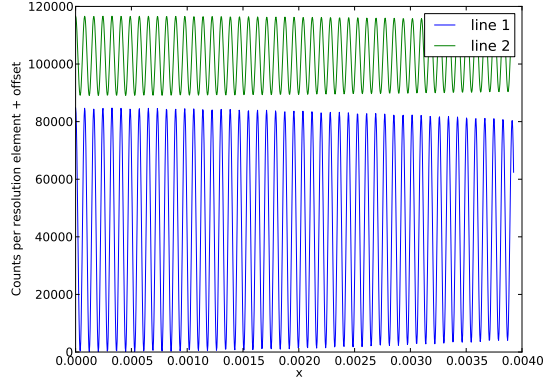


Fig. 6.— The output signal for positive x of the SHS configuration $\sigma_0 = (\sigma_1 + \sigma_2)/2$.

the two signals for an unambiguous measure of the frequency of each. In this article, this scheme is referred to as an External Dispersion SHS (ED-SHS). The observed signal is described by

$$I(\sigma, x) = \frac{1}{\Delta x} \left[\int_{\sigma}^{\sigma \exp(1/2R)} B(\sigma') (1 + \cos(2\pi x(2\sigma' \sin \gamma))) d\sigma' \otimes \text{PSF} \right] \quad (27)$$

The similarities between ED-SHS and EDI can be seen in Fig. 2 of ?; both use interferometry to create wavelength-dependent modulations in the signal, the distinction between the two coming from the functional form of the modulation frequency.

The signal from two columns of pixels corresponding to the two wavelengths of the [OIII] doublet of the SDSS target specified by Plate #1268, Fiber #318 is shown in Figure 6. The Littrow wavelength is set to the average of the two lines $\sigma_0 = (\sigma_1 + \sigma_2)/2$. In an SHS the output signal would be the sum of these and all other columns in the bandpass.

The redshift precisions on the target galaxies are given in Table 3. The statistical uncertainties are improved compared to those of the SHS, and are comparable to the performance of the EDI.

Now that the signals from different wavelengths are no longer mixed, calibration arcs can be observed with the science image without increasing the photon noise of the doublet lines. Both wavelength and PSF calibration are simplified as with the EDI. In addition, the flux signals are further reduced relative to the SHS relaxing flux calibra-

tion requirements.

6.5. Misc

Maybe these instruments are good for atomic line catalogs.

7. Conclusions

[EL: Revise Conclusions once article integrated.] The three cosmic probes of redshift drift described here offer great advantages over the brute force method. Differential radial baryon acoustic oscillations take advantage of large number statistics, should achieve drBAO accuracy of a couple percent (otherwise requiring 50 years for a redshift sensitivity of 10^{-10}), and come for free with planned redshift surveys. Cosmic pulsars, for example supermassive black hole binaries rather than pulsars, would be highly robust and leverage multiple signals per source. Again, these will be followed automatically with gravitational wave searches and the concomitant searches for electromagnetic counterparts. Strongly lensed time varying sources, such as quasars, allow for simultaneous differential redshift measurement “all in one night”, ameliorating systematics and allowing the universe to do the work of providing a long baseline in time.

Perhaps it is not too much of a dream that upcoming all sky surveys in the time domain could find “golden” sources such as a lensed cosmic pulser or $\gtrsim 3$ y time delay strong lens. These would be extraordinary cosmographic tools.

In the categorization of ?, we have here tried to replace patience (of decade time scales) with clever ideas on how to get the universe and astrophysics to work for us. These methods also have considerable synergy with surveys already planned for different purposes, and so mostly involve only different analysis or minor instrumentation. The surveys, and the universe, provide the “1000 nights” and redshift drift cosmologists need only add the “1 night”.

We are grateful to Jerry Edelstein for useful discussions on EDI. AGK thanks the Institute for the Early Universe, Korea and EVL thanks the Korea Astronomy and Space Science Institute for hospitality. This work has been supported by DOE grant DE-SC-0007867 and the Director, Office of

Science, Office of High Energy Physics, of the U.S. Department of Energy under Contract No. DE-AC02-05CH11231.